Activity-based urinary biomarkers of response and resistance to checkpoint blockade immunotherapy

Authors: Quoc Mac[1], Congmin Xu[1], James R Bowen[1], Anirudh Sivakumar[1], Hathaichanok Phuengkham[1], Fang-Yi Su[1], Samuel Z. Stentz[1], Hyoungjun Sim[1], Adrian M. Harris[1], Tonia T. Li[1], Peng Qiu[1,2,5], Gabriel A. Kwong[1–6,*]

Affiliations:

[1]Wallace H. Coulter Department of Biomedical Engineering, Georgia Tech College of Engineering and Emory School of Medicine, Atlanta, GA 30332, USA.

[2]Parker H. Petit Institute of Bioengineering and Bioscience, Atlanta, GA 30332, USA.

[3]Institute for Electronics and Nanotechnology, Georgia Tech, Atlanta, GA 30332.

[4]Integrated Cancer Research Center, Georgia Tech, Atlanta, GA 30332.

[5]The Georgia Immunoengineering Consortium, Emory University and Georgia Tech, Atlanta, GA 30332.

[6]Winship Cancer Institute, Emory University, Atlanta, GA 30322

[*]To whom correspondence should be addressed: gkwong@gatech.edu (G.A.K.)

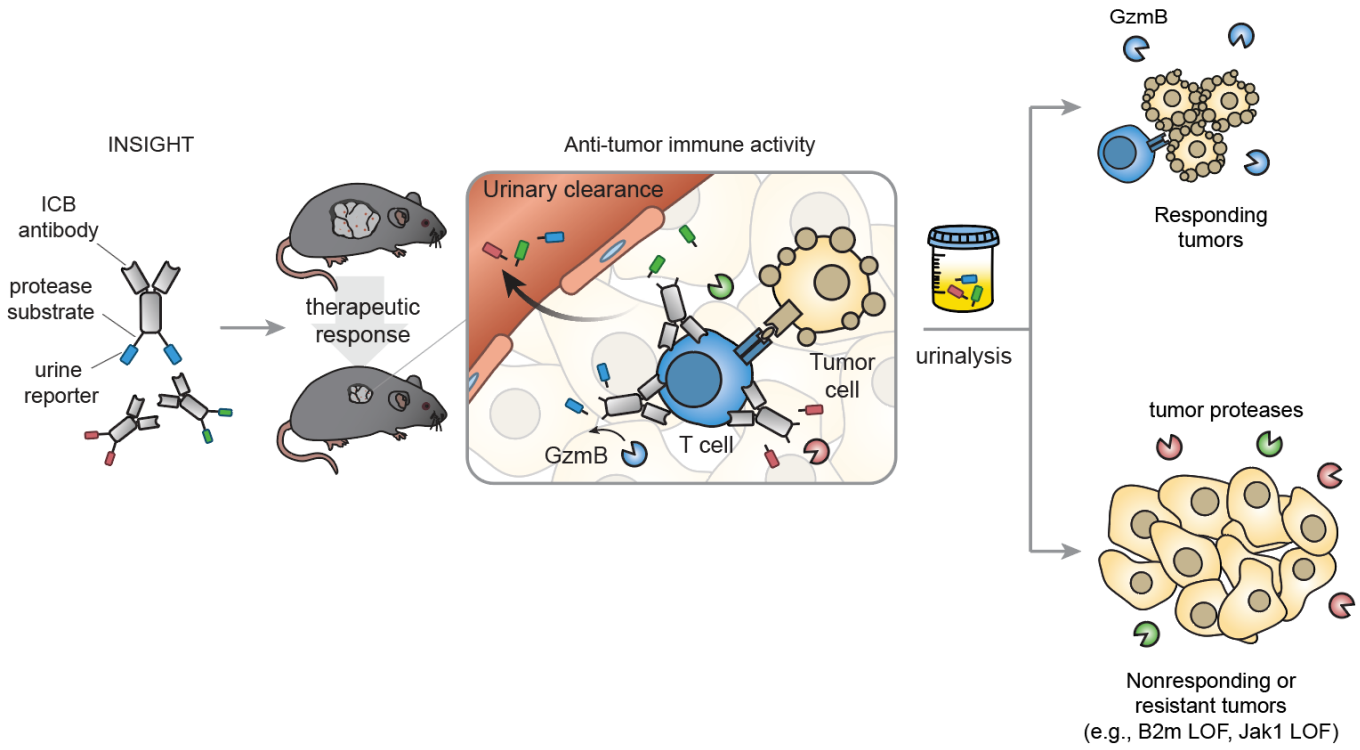

Abstract

Immune checkpoint blockade (ICB) therapy has transformed the clinical care of cancer, yet the majority of patients do not derive clinical benefit and responders can acquire resistance to therapy. Noninvasive biomarkers to indicate early on-treatment response and resistance mechanisms are needed to improve patient management. We engineer activity-based synthetic biomarkers called immune sensors for monitoring checkpoint blockade therapy (INSIGHT), which comprise a library of mass-barcoded peptides conjugated to ICB antibodies (e.g., αPD1). INSIGHT allows detection of *in vivo* T cell and tumor protease activity by quantification of cleaved peptide fragments that have cleared into urine. αPD1-sensor conjugates monitoring the T cell protease granzyme B (GzmB) retained target binding and were capable of sensing T cell killing of cancer cells. In syngeneic tumors, systemic administration of these conjugates resulted in therapeutic efficacy comparable to unconjugated antibodies and produced elevated reporter signals in urine indicative of tumor responses by the second dose. To differentiate resistant tumors, we analyzed the transcriptomes of ICB-treated tumors for protease signatures of response and resistance and developed a multiplexed library of mass-barcoded protease sensors. This library enabled us to build machine learning classifiers based on urine signals that detected and stratified two mechanisms of resistance, B2m and Jak1 loss-of-function mutations. Our data demonstrates the potential of INSIGHT for early on-treatment response assessment and classification of refractory tumors based on resistance mechanisms.

Introduction

Immune checkpoint blockade (ICB) therapy has transformed the treatment of cancer for patients across a broad range of malignancies[1,2]. ICB involves the administration of antibodies that block inhibitory checkpoint molecules, such as the cytotoxic T lymphocyte-associated protein 4 (CTLA-4) or the programmed cell death 1 (PD-1), to invigorate an anti-tumor T cell response. Since the approval of ipilimumab (αCTLA-4) for the treatment of melanoma in 2011, seven ICB biologics have been approved by the FDA as part of standard of care for patients with advanced tumors, including non-small cell lung cancer, head and neck cancer, and metastatic colorectal cancer. Despite the potential to produce durable clinical outcomes, a large fraction of patients do not benefit from ICB therapy and responders acquire resistance over the course of treatment[1,3]. Identification of pharmacodynamic (PD) biomarkers to assess immune responses and classify resistant tumors early on-treatment has emerged as a clinical priority.

Currently, tumor responses to ICB therapy are assessed using a combination of radiologic imaging, tumor biopsies, and blood tests[4]. Radiologic imaging consists of monitoring changes in tumor dimension and classifying patients into response categories according to evaluation criteria such as RECIST, irRC, or irRECIST. The kinetics and patterns of response to ICB therapy, consisting of delayed objective responses and atypical phenomena (e.g., pseudoprogression, hyperprogression), are different than that of conventional cytotoxic therapies and can complicate clinical interpretation by imaging[4,5]. Complementary to imaging data, longitudinal tumor biopsies and blood tests offer clinical insights into the immunological changes of the tumor and peripheral blood

during the course of treatment. Analyses of core tumor biopsies from ICB-treated patients have shown that patient prognoses correlate with T cell activity, such as high density of CD8+ T cells with elevated expression of IFNγ and granzymes, low density of regulatory T cell, and high expression of IFNγ-induced PD-L1 in tumor cells[2,6]. Additionally, genomic analyses of tumor biopsies revealed that mutations in antigen processing (e.g., TAP1, TAP2), antigen presentation (e.g, B2m), and interferon signaling (e.g., JAK1, JAK2) contribute to tumor-intrinsic resistance to ICB therapy[3,7]. Immune analyses of peripheral blood discovered potential biomarkers for response to ICB, including soluble proteins (e.g., LDH, sCD25, IL-8) and cellular composition (e.g., absolute lymphocyte count, CD45RO+CD8+ count, neutrophil-to-lymphocyte ratio)[4]. These findings highlight the potential of biomarkers that probe immune activation and the tumor microenvironment to accurately predict patient responses to ICB therapy

Proteases provide a unique opportunity for the evaluation of ICB therapy due to their fundamental role in tumor biology, immunity, and anti-tumor responses. Tumor-associated proteases are involved in proteolytic cascades that modify the tumor microenvironment (TME) during angiogenesis, growth, and metastasis[8]. In addition, T cell-mediated tumor control centers on a protease-driven process that includes secretion of granzymes by cytotoxic T cells and activation of caspases to mediate cancer cell death [9]. Consequently, these protease signatures can be used to track tumor progression and regression, monitor anti-tumor immune activities, and provide early indications of therapeutic response and resistance during ICB therapy[10–15]. Of note, the cytolytic score, defined as the geometric mean of the expression of granzymes and perforin, is associated with tumor mutation burden (TMB) and response to αCTLA-4 in metastatic melanoma[16].

Prodrugs and diagnostics that exploit tumor- and immune-associated proteases are being evaluated in clinical trials, including masked ICB antibodies, which bind to inhibitory targets after cleavage by tumor-secreted matrix metalloproteases (MMPs)[17], and GzmB-PET, which labels the active form of GzmB in the tumors for response monitoring[14]. Furthermore, nanoparticles monitoring the activity of GzmB enabled noninvasive detection of anti-graft T cell response in a mouse model of skin transplantation[18]. Motivated by these works, we hypothesized that quantifying the activity of tumor and T cell proteases during ICB treatment may enable detection of therapeutic responses and classification of resistant tumors.

Here we engineered INSIGHT, immune sensors for monitoring checkpoint blockade therapy, as a noninvasive technology that provides diagnostic insights into patient immune responses and resistance during ICB treatment. In INSIGHT, each αPD1- or αCTLA4-sensor conjugate consists of protease-sensing peptides coupled to the antibody scaffold. Treatments with these conjugates enable local cleavage of peptide substrates by proteases in the TME, releasing terminal reporters that are remotely filtered into urine for noninvasive detection of tumor responses. We first developed αPD1-GzmB sensor conjugates that retained target binding to PD1 ligand while being capable of sensing T cell-mediated killing of cancer cells. In tumor models of ICB response, these conjugates produced increased urine signals to detect early on-treatment therapeutic responses. By analyzing the transcriptomes of ICB-treated mouse and human tumors, we identified protease signatures of tumor response and resistance, which motivated the development of a multiplexed library of mass-barcoded protease sensors for comprehensive response assessment during ICB therapy. In mice bearing responsive

wild-type (WT) tumors or resistant knockout (KO) tumors, systemic administration of this library enabled us to build urinary classifiers that segregated WT responders, B2m loss resistance, and Jak1 loss resistance with high diagnostic validity. Our data demonstrate the potential of INSIGHT for monitoring therapeutic responses and classifying underlying resistance mechanisms.

Results

Antibody-peptide sensor conjugates retain target binding and in vivo therapeutic efficacy

We first sought to characterize target binding and therapeutic efficacy of antibody-peptide conjugates for use in INSIGHT. αPD1-GzmB sensor conjugates (αPD1-GS) were formulated by coupling fluorescently labeled peptide substrates for murine GzmB (IEFDSG[18]) to the antibody using a heterobifunctional linker (**Fig. 1a**). To ensure that peptide conjugation did not interfere with PD1 binding, we optimized the ratio of peptide to antibody using an ELISA with recombinant PD1 protein. We found that target binding of mouse αPD1-GS (clone 8H3) was reduced, with an increase of EC50 constants from 6.36 nM to 24.0 nM, as we increased the valency of peptide to antibody from 1 to 7 (**SFig. 1a**). Since the conjugate with 1:1 valency had negligible reduction in target binding relative to that of the unconjugated antibody (EC50 = 3.6 nM vs. 2.1 nM), we decided to use this conjugation condition in subsequent studies (**Fig. 1b**). To test whether this valency is applicable for other therapeutic antibodies, we coupled peptides to another αPD1 clone (29F.1A12) and found that target binding was preserved between αPD1-GS and unconjugated antibody (EC50 = 0.15 nM vs. 0.18 nM) (**Fig. 1c**). Since ligand presentation of plate-bound recombinant PD1 differed from that of endogenous PD1 expressed on cell surface, we next evaluated target binding of αPD1-GS to tumor infiltrating lymphocytes (TILs) extracted from MC38 tumors. We used the MC38 colon adenocarcinoma syngeneic tumor model because these cancer cells have a high mutation burden, which has been shown to recruit a natural infiltrate of T cells required for an effective anti-tumor response following αPD1 monotherapy[19]. Flow cytometry analysis of CD8+ TILs stained with either αPD1-GS or unconjugated αPD1 showed

156 statistically equivalent PD1 expression by median fluorescence intensity (MFI),
157 demonstrating that peptide conjugation did not significantly affect target binding to
158 endogenous PD1 ligand expressed on cell surfaces (n = 10, **Fig. 1d, e**). Finally, to directly
159 compare *in vivo* therapeutic efficacy of αPD1-GS to αPD1, we administered each
160 formulation to mice bearing MC38 tumors. Systemic injections of αPD1-GS significantly
161 enhanced tumor control relative to IgG1 isotype control antibody and resulted in no
162 statistical difference in tumor burden compared to unconjugated αPD1 ($P \leq 0.0001$, n =
163 6, **Fig. 1f**). Taken together, these data demonstrate that relative to unconjugated
164 antibody, αPD1-peptide conjugates preserved both target binding on CD8+ T cell
165 surfaces and *in vivo* therapeutic efficacy.
166
167
168
169
170
171
172
173
174
175
176
177
178

Antibody-sensor conjugates monitor GzmB activity during T cell killing of tumor cells

To investigate whether the antibody-peptide conjugates could monitor protease activity, we sought to evaluate GzmB substrate cleavage on αPD1-GS and assess its potential for monitoring anti-tumor T cell killing *in vitro*. To quantify GzmB cleavage as a measure of sensor activation, we incorporated an internal dark quencher on one end of the peptide substrate, whose cleavage releases a terminal fluorescent reporter to substantially enhance sample fluorescence (**Fig. 2a**). We first assessed substrate specificity for GzmB by exposing αPD1-GS to fresh mouse serum, tumor-associated proteases (e.g., cathepsin B, MMP9), or coagulation and complement proteases (e.g., C1s, thrombin). When αPD1-GS was incubated with mouse serum or recombinant proteases, we did not observe detectable increases in fluorescence that would indicate cross-cutting of our sensors (**Fig. 2b**). Conversely, incubation with GzmB produced a 22-fold increase in sensor fluorescence intensity. To evaluate the ability of our sensors to detect GzmB activity by T cells, we used a T cell killing assay in which transgenic Pmel T cells recognize the gp100 antigen expressed on B16 melanoma cells (**Fig. 2a**). Because our sensors were engineered to detect GzmB activity, we first quantified the amount of extracellular GzmB in coculture supernatants by ELISA and detected a 10-fold increase in GzmB levels as the ratio of T cells to target cells was increased from 1 to 10 ($P \leq 0.0001$, n = 3, **Fig. 2c**). Next, to characterize target cell cytotoxicity in cocultures with T cells, we quantified the activity of lactose dehydrogenase (LDH), a cytosolic enzyme rapidly released upon damage to the cell membrane. We detected a significant increase in cytotoxicity from 13 to 56 % as the ratio of Pmel T cells to B16 target cells was increased from 1 to 10 ($P \leq 0.001$, n = 3, **Fig. 2c**). To test background sensor activation by either

tumor cells or T cells alone, we incubated αPD1-GS with media control, MC38 and CT26 colon carcinoma cells, B16 melanoma cells, and activated Pmel T cells with or without target cells. We observed that both tumor cells and activated Pmel T cells did not significantly activate the GzmB sensors as measured by sample fluorescence. By contrast, coincubation of Pmel T cells with B16 target cells significantly increased this activation signal up to 4.6-fold ($P \leq 0.0001$, $n = 3$, **Supplemental Fig. 2**). To assess the ability to monitor T cell killing, we coincubated Pmel T cells with B16 target cells at various ratios and spiked in either αPD1-GS, an αPD1-sensor with a control peptide substrate lacking GzmB cleavage motif, or unconjugated αPD1 antibody. Whereas the αPD1-sensor control and unconjugated αPD1 antibody did not produce detectable increases in fluorescence, αPD1-GS was markedly activated in all coculture conditions, with fluorescent signals increasing by more than 4-fold as we increased the Pmel to B16 ratio from 1 to 10 ($P \leq 0.0001$, $n = 3$, **Fig. 2e**). Lastly, we investigated the utility of our sensors to monitor antigen-specific T cell killing in cocultures of B16 target cells with Pmel or control OT1 T cells. While the OT1 cocultures did not produce significant increases in sensor fluorescence at the 10:1 ratio of OT1 T cells to B16 target cells, Pmel cocultures activated our sensors at all ratios ($P \leq 0.0001$, $n = 4$, **Fig. 2f**). Collectively, these data demonstrate that αPD1-GS was cleaved selectively by GzmB and can be used to detect antigen-specific T cell killing of tumor cells.

Noninvasive detection of early on-treatment response to ICB therapy

Conjugation of peptides to antibody has been shown to extend the circulation half-life of free peptides without affecting that of the antibody carrier[17,20]. We therefore investigated whether the circulation of GzmB-sensing peptides was improved upon conjugation by determining the half-life of intact αPD1-GS in naïve mice. To quantify the serum concentration of αPD1-GS, we developed a sandwich ELISA that requires binding to both recombinant PD1 ligand and the FITC reporter on the peptide to produce a detection signal (**Supplemental Fig. 3a**). We observed that αPD1-GS produced significantly higher absorbance signals relative to unconjugated αPD1 antibody ($P \leq 0.001$, $n = 3$), and incubation with GzmB significantly decreased this signal up to 4-fold, due to the cleavage of FITC-labelled peptides ($P \leq 0.001$, $n = 3$, **Supplemental Fig. 3b, 3c**). Using this assay, we determined that the circulation half-life of αPD1-GS was not statistically different than that of unconjugated αPD1 antibody (6.5 ± 4.2 h vs 3.9 ± 1.3 h, $n = 3$) and consistent with reported values for αPD1 antibodies[21]($n = 3$, **Fig. 3a**).

Patient responses to ICB can have aberrant kinetics, with positive responses and hyperprogression having been observed after one or two doses[22,23]. Since early detection of therapeutic outcomes has the potential to improve patient management, we sought to investigate the utility of INSIGHT probes for monitoring tumor responses after the first few ICB doses. We first administered αPD1-GS or matched isotype control (Iso-GS) to C57BL/6 mice bearing MC38 tumors. To characterize the expression of GzmB during the early course of ICB treatment, we isolated TILs after two doses of antibody and analyzed CD8+ T cells by flow cytometry. We observed that mice treated with αPD1 had significant increases in GzmB+ CD8+ TILs relative to those treated with isotype control ($P \leq 0.001$,

n = 9, **Fig. 3b, c**). These results were consistent with previous mouse and human studies and supported the role of GzmB-mediated tumor control in T cell responses after ICB treatment[16,24]. Additionally, serial treatments with αPD1-GS significantly lowered MC38 tumor burden relative to the control treatment after two doses ($P \leq 0.001$, n = 6, **Fig. 3d**). To evaluate the potential for serial on-treatment response assessment, we analyzed the concentration of the cleaved reporter in urine samples after each dose of administration. After the first dose, there was no statistical difference in urine signals of mice treated with either αPD1-GS or Iso-GS. By contrast, urine signals were significantly elevated in αPD1-GS-treated mice after the second ($P \leq 0.01$, n = 7) and third doses ($P \leq 0.0001$, n = 7), detecting GzmB activity two days before tumor burden significantly diverged between αPD1-GS-treated and Iso-GS-treated mice (**Fig 3e**). This elevation in urine signals corresponded with a diagnostic AUROC of 0.86 and 1.00 on the second and third doses, respectively.

To evaluate whether ICB-sensor conjugates can detect therapeutic responses during combination therapy, we tested their performance in BALB/c syngeneic CT26 tumors, which have shown better responses to ICB combination relative to monotherapy[25,26]. Relative to matched isotype control conjugates, serial treatments with either αPD1-GS or αCTLA4-GS did not result in statistical differences in tumor burden and urine signals after all doses of administration (**Supplemental Fig. 4a, b, c, d**). By contrast, combination treatments with of αPD1-GS and αCTLA4 resulted in significantly lower tumor burden ($P \leq 0.0001$, n = 6, **Fig. 3f**) and higher levels of GzmB+ CD8+ TILs ($P \leq 0.05$, n = 7, **Supplemental Fig. 5a, b**). Additionally, urine signals were significantly elevated by the second dose in combination therapy-treated mice relative to the control

group (AUROC > 0.9), three days before tumor burden was statistically different between the two groups ($P \leq 0.0001$, $n = 6$, **Fig. 3g**). Collectively, these results demonstrate that systemic administration of αPD1-GS enabled noninvasive detection of therapeutic responses within the first two doses of treatment with high diagnostic sensitivity and specificity.

Modelling resistance to ICB therapy by targeted gene knockout

Early detection of primary and acquired resistance has the potential to improve the clinical decision-making during ICB therapy. Tumors become resistant to checkpoint inhibitors by disrupting pathways related to the initiation and maintenance of an effective anti-tumor T cell response, including loss-of-function mutations in B2M, a protein subunit of MHC-I, or JAK1, an essential signaling protein of the IFNγ response pathway[3,7]. As genetic disruptions in these important immune genes lead to marked changes in the tumor behaviors and anti-tumor immunity, tumor- and immune-associated proteases are potentially dysregulated. To assess the potential of INSIGHT to sense dysregulated proteases in the context of ICB resistance, we developed $B2m^{-/-}$ and $Jak1^{-/-}$ tumor models and established their susceptibility to ICB therapy.

To model the resistant phenotypes observed in human tumors, we used CRISPR/Cas9 to knock out B2m and Jak1 from wildtype (WT) MC38 tumor cells. We first validated the knockout efficiency by TIDE (Tracking of Indels by Decomposition) analysis[27] of sequencing data (**Supplemental Fig. 6a**). To assess the functional consequence of $B2m^{-/-}$, we analyzed surface expression of the MHC-I molecule H2-Kb and found that its expression was markedly lower in $B2m^{-/-}$ relative to WT or $Jak1^{-/-}$ cells (**Supplemental Fig. 6b**). In addition, to determine whether $B2m^{-/-}$ cells were resistant to T cell killing, we performed T cell killing assays using transgenic OT1 T cells and WT or $B2m^{-/-}$ MC38 target cells pulsed with the cognate antigen ovalbumin (OVA). Relative to WT cells, $B2m^{-/-}$ target cells induced significantly lower expression of GzmB and IFNγ in cocultured OT1 T cells ($P \leq 0.05$, $n = 3$, **Fig. 4a**). To assess the functional consequences of $Jak1^{-/-}$, we coincubated WT, $B2m^{-/-}$, and $Jak1^{-/-}$ cells with IFNγ and evaluated the

effect of IFNγ stimulation on expression of H2-Kb and PD-L1, downstream effectors of the IFNγ signaling pathway[28]. In the presence of IFNγ, WT MC38 tumor cells significantly increased expression of both MHC-I and PD-L1 ($P \leq 0.0001$, $n = 3$, **Fig. 4b**, **Supplemental Fig. 6c**). By contrast, $B2m^{-/-}$ cells only upregulated expression of PD-L1 ($P \leq 0.0001$, $n = 3$), and $Jak1^{-/-}$ cells did not have significant increases in either MHC-I or PD-L1 expression. Overall, these data showed that $B2m^{-/-}$ cells had impaired antigen presentation whereas $Jak1^{-/-}$ cells were insensitive to IFNγ stimulation.

To investigate whether knockout tumors are resistant to ICB therapy, we implanted mice with WT, $B2m^{-/-}$, and $Jak1^{-/-}$ MC38 tumors and treated them with either αPD1 or IgG1 isotype control. Serial αPD1 treatments resulted in significantly smaller tumors and improved survival of WT tumor-bearing mice (MST = 30) relative to the isotype control (MST = 21) ($P \leq 0.0001$, $n = 25$, **Fig. 4c, d**). Conversely, αPD1 treatments did not result in statistical differences in tumor burden and overall survival in mice with $B2m^{-/-}$ and $Jak1^{-/-}$ tumors. To characterize T cell responses in B2m and Jak1 resistant tumors, we performed flow cytometry analysis of CD8+ TILs in all treatment groups. We found significant increases in the populations of GzmB+ and CD44+PD1+ (antigen-experienced) CD8+ TILs in αPD1-treated relative to isotype-treated WT tumors ($P \leq 0.01$, $n = 5$, **Fig. 4e, f**). By contrast, αPD1 treatments did not cause an increase in these populations in $B2m^{-/-}$ and $Jak1^{-/-}$ tumors. Taken together, our results demonstrate that loss-of-function mutation in B2m or Jak1 impaired induction and maintenance of an effective anti-tumor T cell response, which rendered MC38 tumors resistant to αPD1 therapy.

Identification of protease signatures in ICB response and resistance

To detect therapeutic response and differentiate resistance mechanisms, we sought to identify the proteases that are associated with ICB response and resistance. We achieved this by sequencing mRNA (RNA-Seq) from WT, B2m$^{-/-}$, and Jak1$^{-/-}$ MC38 tumors treated with either αPD1 or IgG1 isotype control. Global gene expression analyzed by t-SNE plot revealed different transcriptional profiles of the three tumor types (**Fig. 5a**). Furthermore, treated WT tumors clustered separately from untreated tumors while no clear separation was observed for treated resistant tumors. Transcript levels of B2m and Jak1 were significantly lower in their respective knockout tumors, which further validated the efficiency of the knockout ($P \leq 0.0001$, $n = 5$, **Supplemental Fig. 7**). To evaluate the functional consequences of αPD1 treatment and gene knockout on each tumor, we performed gene set enrichment analyses (GSEA) on the Hallmark gene sets[29], using isotype-treated WT tumors as the control group. Treatment with αPD1 significantly enriched the immune pathways (e.g., IFNγ response, IL2-STAT5 signaling, inflammatory response, complement) in WT tumors but not in B2m$^{-/-}$ and Jak1$^{-/-}$ tumors ($P \leq 0.05$, **Fig. 5b**, **Supplemental Fig. 8a**), validating the presence of an active immune response in response to αPD1 treatment in WT tumors. Relative to WT and B2m$^{-/-}$ tumors, Jak1$^{-/-}$ tumors significantly downregulated the IFNγ response pathway. Furthermore, gene set signatures related to both pro-tumor (e.g., Myc targets, Epithelial mesenchymal transition) and immune processes were distinct between the knockout tumors (**Supplemental Fig. 8c**), indicative of unique mechanisms regulating resistance. To assess the relevance of our model of ICB response, we next performed GSEA on bulk tumor RNA-Seq data from advanced melanoma patients treated with αPD1 monotherapy[24]. Patient samples were

separated into responders (CR + PR), non-responders (PD), and stable disease patients (SD) based on RECIST response criteria. Relative to non-responders, the responders had significant enrichment in 5 out of 7 Hallmark immune pathways, indicative of productive anti-tumor immune responses ($P \leq 0.05$, **Fig. 5b, Supplemental Fig. 8b**). The observed conservation between mouse and patient data demonstrates that our model recapitulated clinically relevance gene signatures of ICB response.

We next performed differential expression analysis to identify proteases involved in ICB response and resistance. Relative to isotype control, αPD1 treatment induced significant upregulation of multiple proteases, including granzymes, metalloproteinases, and cathepsins in WT tumors ($P \leq 0.05$, **Fig. 5c, Supplemental Fig. 9a**). Additionally, analysis on resistant tumors revealed multiple protease classes that were differentially expressed in αPD1-treated $B2m^{-/-}$ vs. $Jak1^{-/-}$ tumors ($P \leq 0.05$, **Fig. 5d, Supplemental Fig. 9b**). To validate the clinical relevance of these protease classes, we performed a similar analysis on the human data set of advance melanoma patients[24]. As observed in our mouse models, human tumors that responded to ICB (CR + PR) underwent significant upregulation of granzymes, metalloproteases, cathepsins, complement, and coagulation proteases relative to non-responders (PD) ($P \leq 0.01$, **Fig. 5e, Supplemental Fig. 9c**). Taken together, these data revealed that proteases are differentially regulated in the context of tumor response and resistance. Consequently, targeting major classes of tumor and immune proteases with INSIGHT has the potential to monitor therapeutic response and classify underlying resistance during ICB therapy.

Machine learning classification of ICB response and resistance by multiplexed activity sensors

Here we wanted to design a multiplexed library of antibody-activity sensor conjugates that produce urinary reporter signals based on which machine learning classifiers of ICB response and resistance can be built (**Fig. 6a**). After identifying the families of immune and tumor proteases to target, we sought to optimize peptide substrates that monitor representative proteases from these families. To do this, we first selected a library of potential substrates from the literature and validated their cleavage efficiency in protease activity assays. We incubated each fluorescently quenched substrate with the representative proteases and measured cleavage activity by monitoring the change in fluorescence over time (**Supplemental Fig. S10a**). With this screen, we identified 14 peptide substrates (**Table S1**) that encompass cleavage preferences of the five target protease families (**Fig. 6b, Supplemental Fig. S10b**). While few substrates are specific for an individual protease or family of proteases (e.g. L2-1, L3-7, L2-21), many substrates were cleaved by proteases of multiple families. The latter observation indicates the promiscuous nature of proteolysis[30] and highlights the importance of monitoring multiple families of proteases with multiple substrates to capture the complexity of protease biology in response and resistance to immunotherapy. Moreover, the cleavage signatures of this set of substrates were not strongly correlated (correlation constants of most substrate pairs < 0.8), justifying their inclusion in our library of protease sensors (**Fig. 6c**). To enable multiplexed detection of protease activity, we labeled the chosen substrates with isobaric mass barcodes, which are isotopically labeled Glufib peptides that share the same MS1 parent mass for reporter pooling but produce unique fragmented

MS2 ions distinguishable by tandem mass spectrometry (MS/MS)[10]. After coupling individual mass-barcoded substrate to αPD1 or IgG1 antibody, we prepared the 14-plex library of antibody-activity sensor conjugates by mixing either αPD1 or IgG1 formulations at equimolar concentrations. LC/MS-MS analysis of the conjugate mixtures resolved the mass reporters to individual contributions, facilitating multiplexed detection of protease activity (**Supplemental Fig. S11**).

We next sought to perform longitudinal response assessment during ICB therapy by treating WT, B2m$^{-/-}$, and Jak1$^{-/-}$ tumor-bearing mice with INSIGHT library of either αPD1 or IgG1 conjugates. To establish the diagnostic utility of our multiplexed sensors, we leveraged machine learning to build binary classifiers based on urinary reporter signals at early treatment time points that could be applied to discriminate αPD1-treated from IgG1-treated WT tumors for response monitoring, or αPD1-treated B2m$^{-/-}$ from αPD1-treated Jak1$^{-/-}$ tumors for resistance stratification. To evaluate classification robustness and minimize bias in data splitting for training and testing purpose, we split the data into training and test sets using 5-fold cross validation and repeated this procedure 100 times to obtain the average area under the ROC curve (AUC) for all test results (ref). For monitoring therapeutic response, we built random forest classifiers on urine signals from αPD1-treated WT tumors (n = 25) and IgG1-treated controls (n = 15). Our classifiers differentiated treated mice from isotype-treated controls with high diagnostic accuracy as early as the second dose of treatment ($AUC_{dose\ 2}$ = 0.92, $AUC_{dose\ 3}$ = 0.93) (**Fig. 6d**). When we used the classifier trained on dose 3 signals to classify based on dose 2 signals, a comparable diagnostic performance was achieved ($AUC_{trained\ dose\ 3,\ tested\ dose\ 2}$ = 0.88), indicating that the urine signatures were consistent across the two

doses (**Supplemental Fig. S12a**). To evaluate the contribution of individual probes to this response monitoring classification, we obtained feature importance scores from the random forest classifiers. We found a set of three probes (L2-8, L3-7, and L2-1) contributing markedly more than others in the classification performance (**Fig. 6e**). Where L2-1 monitored granzymes and specifically GzmB, L2-8 monitored matrix metalloproteases and cathepsins. This set of probes provided coverage for all three protease families differentially expressed between the two groups based on RNA data (**Fig. 5c**). To assess the utility of INSIGHT in stratifying refractory tumors based on resistance mechanisms, we next built classifiers to distinguish αPD1-treated $B2m^{-/-}$ (n = 15) from $Jak1^{-/-}$ tumors (n = 15). We achieved good classification performance and an increase in diagnostic accuracy when using urine signals on dose 3 as compared to dose 2 ($AUC_{dose\ 2}$ = 0.77, $AUC_{dose\ 3}$ = 0.91) (**Fig. 6f, Supplemental Fig. S12b**). Moreover, feature importance analysis showed multiple probes contributing almost equally to resistance stratification, with the top 8 performing probes monitoring all 5 target protease families (**Fig. 6g**).

While a full set of 14 probes was used in our studies, it is possible that smaller probe sets could accurately classify ICB response or stratify resistance mechanisms, allowing customization of INSIGHT based on intended use cases. To investigate this utility, we built response monitoring classifiers using the three most important probes from the feature importance analysis. We found that these classifiers produced comparable diagnostic performance ($AUC_{dose\ 2}$ = 0.95, $AUC_{dose\ 3}$ = 0.91) to those trained on signals from the entire INSIGHT panel (**Fig. 6h, Supplemental Fig. S13a**). For resistance stratification, we built classifiers in an iterative basis by adding one probe at a time

following a descending order of importance. By this analysis, we found that the diagnostic AUCs reached saturated values when using the 5 probes with highest importance scores (L2-11, L2-20, L2-19, L3-16, and L2-9) to build the classifiers ($AUC_{dose\ 2}$ = 0.80, $AUC_{dose\ 3}$ = 0.91) (**Fig. 6h, Supplemental Fig. S13b, c**). Of note, there was no overlap between the set of response monitoring probes and resistance stratifying probes. Furthermore, by feature importance scores, the three response monitoring probes were among the least important probes for resistance stratification, and vice versa (**Fig. 6i**). The former observation indicated that probes that are important for monitoring therapeutic response are less useful for discriminating the two resistant tumors, in which there were no active anti-tumor immune responses. Overall, our results demonstrate the potential of integrating multiplexed antibody-activity sensor conjugates with machine learning for noninvasive longitudinal monitoring of response and resistance to ICB therapy.

Discussion

In this study, we developed antibody-activity sensor conjugates consisting of ICB antibodies decorated with protease-sensing peptides, termed INSIGHT, to monitor immune responses during treatment. Early response assessments that detect therapeutic responses and differentiate resistance mechanisms during ICB therapy have the potential to generate diagnostic insights to facilitate better treatment decisions. In mice bearing tumors that respond to ICB therapy, systemic administration of conjugates monitoring the activity of GzmB produced elevated reporter signals in urine, indicating therapeutic responses noninvasively as early as on the second dose of treatment. By analyzing the transcriptomes of ICB-treated murine tumors, we identified protease signatures of therapeutic response consistent with human data and characterized proteases associated with tumor resistance. To stratify ICB resistant tumors, we built a multiplexed library of mass barcoded antibody-sensor conjugates to detect these protease signatures and produce urine signals quantifiable by mass spectrometry. In wildtype and knockout tumor models, we demonstrated that machine learning classifiers trained on urine samples detected on-treatment responders as early as the second dose and stratified B2m loss from Jak1 loss resistance.

We engineered INSIGHT based on our work on synthetic biomarkers, which are composed of activity-based biomarkers that monitor dysregulated protease activities for early disease detection in bacterial infection[31], thrombosis[32], cancer[10,11,33], and organ transplant rejection[18]. Previous synthetic biomarkers rely on nanoparticle or polymeric carriers to prevent rapid renal clearance of free peptides, but their utility to target specific disease sites has not been explored. INSIGHT utilizes the extended circulation half-life of

498 therapeutic antibodies while simultaneously harnessing their ability to bind to biological
499 targets and exert therapeutic responses. Conjugation of GzmB peptide substrates to
500 αPD1 antibody extended the circulation half-life of the free peptides ($t_{1/2}$ = 3.9 hour vs.
501 19.2 min[18]) without compromising antibody half-life, consistent with previous reports on
502 the pharmacokinetics of antibody-peptide conjugates[17,20]. Additionally, flow analysis of
503 TILs from murine tumors revealed that αPD1-peptide conjugates can target PD1-
504 expressing CD8+ T cells, which play central roles in anti-tumor immunity reinvigorated by
505 ICB therapy[34]. As cytotoxic CD8+ T cells engage and kill tumor cells, secreted proteases
506 by both immune and tumor cells cleave peptide substrates, releasing reporters that are
507 remotely filtered into urine for noninvasive detection of ICB therapeutic response and
508 resistance. In this study, we showed by multiple metrics, including ELISA, flow cytometry,
509 and *in vivo* studies, that the conjugation of peptides via free lysine side chains did not
510 impact target binding or therapeutic efficacy of ICB antibodies. Our technology could
511 further benefit from site-directed bioconjugation methods, including cysteine-specific
512 reduction, unnatural amino acid incorporation, and enzymatic approaches[35], to produce
513 more consistent formulation with well-defined peptide-to-antibody ratios, thereby
514 improving diagnostic precision. Given that a variety of cargos including peptides have
515 been successfully coupled to therapeutic antibodies[36], we expect that this approach could
516 be extended beyond ICB to benefit other antibody-based therapies.

517 By focusing on monitoring anti-tumor immune activity, INSIGHT demonstrated the
518 potential to detect ICB responses that precede observable changes in tumor burden.
519 Emerging evidence has revealed that dynamic changes in the T cell response can occur
520 early during ICB treatment and are indicative of therapeutic outcomes[22,24,37,38]. In fact,

ICB monotherapy or combination treatments can induce changes in intratumoral[24] and peripheral[22] T cell populations after one dose of treatment (3-4 weeks) that are associated with long-term treatment response and overall survival in advanced melanoma patients. To monitor therapeutic response during ICB therapy, we endowed checkpoint antibodies with the ability to sense GzmB during cytotoxic T cell killing. In two syngeneic tumor models, administration of ICB-GzmB sensor conjugates produced elevated reporter signals in urine of responders as early as the second dose after treatment. These increases in urine signals differentiated ICB-treated responders from isotype-treated controls with high AUROCs (>0.85) before there were significant differences in tumor burden between the two groups. By contrast, when ICB treatment did not induce a therapeutic response, as in CT26 tumors treated with αPD1 or αCTLA4 monotherapy, we did not observe statistical differences in urine signals between treated and control groups. These observations, in addition to the correlation of urine signals to observed increases in GzmB+CD8+ TILs by flow cytometry, indicated that GzmB sensor conjugates could detect early anti-tumor T cell activity reinvigorated by ICB therapy through urinary reporters. When our technology detected the onset of T cell activity on the second dose, this response was primarily induced by the first dose of treatment, as it is unlikely that ICB treatment would induce a therapeutic response within a few hours of urine collection. INISGHT can complement standard of care assessments by radiologic imaging, which are first performed between 9 to 12 weeks (or after at least 3 to 4 ICB doses)[5,39,40], by providing early diagnostic information simply by administering a bolus injection of ICB antibody-sensor conjugates.

Primary refractory tumors and acquired resistance remain the main drivers of patient mortality in ICB therapy[3,7], motivating the need for biomarkers to identify patients with primary resistance or monitor the development of acquired resistance. Our transcriptomic analyses of αPD1 therapy-resistant tumors revealed that protease signatures are markedly different between B2m$^{-/-}$ and Jak1$^{-/-}$ tumors, enabling a mass barcoded library of protease sensors to classify them at early treatment time points. Human tumors acquire resistance to checkpoint inhibitors by mutating important genes of the antigen presentation (e.g., B2M) or IFNγ response (e.g., JAK1, JAK2) pathways to evade CD8 T cell-mediated tumor control[7]. In our study, we generated B2m$^{-/-}$ and Jak1$^{-/-}$ tumor mouse models and validated their resistant phenotypes to aPD1 therapy. Flow cytometry analysis revealed that αPD1 treatments did not induce significant increases in populations of GzmB+ or antigen experienced CD8+ TILs in resistant tumors. This finding indicated that a productive GzmB-mediated T cell response was absent in both tumor types, and a single GzmB sensor was unlikely to be able to differentiate between these two primary resistance mechanisms. Although both knockout tumors were resistant to αPD1 monotherapy, GSEA analysis highlighted different gene set signatures of both immune- and tumor-associated pathways in treated B2m$^{-/-}$ versus Jak1$^{-/-}$tumors, indicating potentially unique biological pathways that regulate the two resistant phenotypes. As proteases play fundamental roles in many immune- and tumor-associated pathways, we showed by differential expression analyses that the proteases signatures were markedly different between B2m$^{-/-}$ and Jak1$^{-/-}$ tumors. Thus, administration of our multiplexed library of protease sensors produced urine signals that could train machine learning classifiers to differentiate these resistant phenotypes

(AUROCs > 0.9). For a biomarker to be clinically useful, there needs to be an improvement in outcomes for those tested positive relative to those with negative results[41]. Despite having high prognostic values, enumeration of circulating tumor cells (CTC) has not been widely adopted as a biomarker for several tumor types (e.g., breast, prostate, colon cancer), as detection of elevated CTC levels did not lead to increased patient survival[42]. In the near future when there are improvements in overall survival for patients with $B2m^{-/-}$ or $Jak1^{-/-}$ tumors, we envision that INSIGHT will allow resistance identification and classification in treatable timeframe, making it valuable as a predictive biomarker.

Materials and Methods

Animals

6- to 8-week old female mice were used at the outsets of all experiments. Pmel (B6.Cg-Thy1a/Cy Tg(TcraTcrb)8Rest/J) and OT1 (C57BL/6-Tg(TcraTcrb)1100Mjb/J) transgenic mice were bred in house using breeding pairs purchased from Jackson Lab. C57BL/6 and BALB/c mice for tumor studies were purchased from Jackson Lab. All animal procedures were approved by Georgia Tech IACUC (protocol #KWONG-A100193).

Antibody-peptide conjugation.

FITC-labelled GzmB substrate peptides ((FITC)AIEFDSGc; lower case letters = d-form amino acids) were synthesized by Tufts University Core Facility and used for *in vivo* formulations. FITC-labelled GzmB substrate peptides with internal quencher ((5-FAM)aIEFDSGK(CPQ2)kkc) were synthesized by CPC Scientific and used for all in vitro activity assays. Peptides with isobaric mass repoters were synthesized in housed using the Liberty Blue Peptide Synthesizer (CEM). Free αPD1 (kind gift of Dr. Gordon Freeman, Dana-Farber) and αCTLA4 (BioXCell; clone 9H10) antibodies were first reacted to the heterobifunctional crosslinker Succinimidyl Iodoacetate (SIA; Thermo, 5:1 molar ratio) for 2 hours at room temperature (RT) in the dark, and excess SIA were removed by buffer exchange using Amicon spin filter (30 kDa, Millipore). Cysteine-terminated peptides were mixed with mAb-SIA (10:1 molar ratio) and reacted overnight at RT in the dark to obtain mAb-peptide conjugate. The conjugates were purified on a Superdex 200 Increase 10-300 GL column using AKTA Pure FPLC System (GE Health Care). Endotoxin was removed from the samples by phase separation with Triton X-114 (Sigma) at 2% final volume ratio (ref). Final endotoxin concentrations were quantified by Pierce LAL Chromogenic Endotoxin Assay Kit (Thermo). Protein concentrations were determined by Pierce Protein Assay Kit (Thermo). Conjugates were buffered exchanged into PBS and sterile filtered before in vivo usage. Conjugation ratios of fluorescently labeled peptides were determined by corrected absorbance measurements by NanoDrop (Thermo). Conjugation of mass-encoded peptides were validated by MALDI using Autoflex mass spectrometer (Bruker).

PD-1 binding.

Binding of αPD1 conjugates to recombinant PD1 ligand was quantified using an ELISA assay developed in house, in which a high protein binding plate was coated with 1 ug/mL of recombinant Mouse PD-1 Protein (R&D, 9047-PD-100). Binding of intact αPD1-GS conjugates was quantified in a sandwich ELISA using the same PD-1 coated plate. After sample incubation, αFITC mAb (Thermo, 13-7691-82; 1:800 dilution staining concentration) was used for secondary staining. ELISA development was performed according to well-established protocol (ref).

Circulation half-life.

For half-life characterization, unconjugated αPD1 or αPD1-GS (100 ug) was administered i.v. to naïve C57BL/6 mice (Jackson Labs). At several time points following administration, blood was collected into Capillary Tubes (VWR), and serum was isolated by centrifugation. Serum concentrations of unconjugated αPD1 and αPD1-GS were determined by the PD1 binding and intact PD1 ELISA respectively.

Recombinant protease cleavage assays

αPD1 was conjugated with GzmB peptide substrates carrying an internal CPQ2 quencher to allow cleavage detection by fluorescent measurements. αPD1-GS (1.3 uM by peptide) was incubated in PBS at 37 °C with fresh mouse serum, murine Granzyme B (0.17 µM; Peprotech), human thrombin (13.5 µM; HaemTech), mouse thrombin (12.5 µM; HaemTech), cathepsin B (1.5 µM, R&D), C1r (1.43 µM; Sigma), C1s (1.80 µM; Sigma), MMP9 (0.1 µM, R&D). Sample fluorescence was measured for 60 minutes using Cytation 5 plate reader (Biotek).

Sensing protease activity during T cell killing

B16-F10 cells (ATCC) were cultured in DMEM supplemented with 10% FBS and 1% penicillin-streptomycin (Thermo). CD8+ T cells were isolated from either OT1 or Pmel (Jackson Labs) splenocytes by MACS using CD8a Microbeads (Miltenyi). Cells were activated by seeding in 96-well plates pre-coated with anti-mouse CD3e (1 µg/ml working concentration, Clone: 145-2C11, BD) and anti-mouse CD28 (2 µg/ml working concentration, Clone: 37.51, BD) at 2×10^6 cells/ml in RPMI 1640 supplemented with 10% FBS, 100U/ml penicillin-streptomycin, 1X non-essential amino acids (Gibco), 1mM sodium pyruvate, 0.05mM 2-mercaptoethanol, and 30U/ml hIL-2 (Roche). After 2 days, cells were washed and transferred to untreated culture flasks for expansion. Between day 4 to 6 after activation, activated T cells were washed before coincubated with $3x10^4$ B16 target cells at various T cell to effector cell ratios. After 48 hours, coculture supernatants were collected for LDH and GzmB measurements by the Pierce LDH Cytotoxicity Assay Kit (Thermo) and GzmB Mouse ELISA Kit (Thermo, BMS6029) respectively. To assess sensor activation during T cell killing, cocultured of T cells and target cells were spiked in with either αPD1-GS, αPD1 conjugated with control peptide (LQRIYK), and unconjugated αPD1. After 48 hours, fluorescence of coculture supernatant were measured using Cytation 5 plate reader (Biotek).

Tumor models

CT26 (ATCC), MC38 (kind gift of the NCI and Dr. Dario Vignali, University of Pittsburgh), and $B2m^{-/-}$ vs. $Jak1^{-/-}$ MC38 tumor cells were cultured in DMEM supplemented with 10% FBS and 1% penicillin-streptomycin (Thermo). Cells were grown to a good density (~70% confluence) before trypsinized for tumor inoculation. On the day of inoculation, C57BL/6 and BALB/c mice were shaved and injected s.c. into the left flank with either $1x10^6$ MC38 or CT26 cells respectively. Tumor burden were monitored until average tumor volume, quantified as 0.52 x length x width x depth, was approximately 100 mm^3 before initiating

665 treatment. Mice were administered with αPD1 and/or αCTLA4 antibody-sensor
666 conjugates or matched isotype control (100-150 ug/injection) every 3 or 4 days.

667

668 *Flow cytometry analysis of intratumoral T cells*

669 Tumor dissociation and staining for flow cytometry. Less than 1g of murine tumors were
670 enzymatically and mechanically dissociated using Mouse Tumor Dissociation Kit
671 (Miltenyi) and gentleMACS Dissociator (Miltenyi). TILs were then isolated from the single
672 cell suspension using a density gradient with Percoll Centrifugation Media (GE Life
673 Sciences) and DMEM Media (10% FBS, 1% Penstrep) at 44:56 volume ratio. TILs were
674 counted with Trypan Blue (Thermo), and approximately $1x10^6$ viable cells per sample
675 were stained for flow cytometry analysis. Cells were first stained for surface markers in
676 FACS Buffer (1x DPBS, 2% FBS, 1 mM EDTA, 25 mM HEPES). Intracellular staining was
677 performed using eBioscience Intracellular Fixation & Permeabilization Buffer Set
678 (Thermo). All antibodies were used for staining at 1:100 dilution from stock
679 concentrations. Stained cells were analyzed by LSRFortessa Flow Cytometer (BD).

680 Antibody clones. CD45 (30-F11), CD8 (53-6.7), CD44 (IM7), PD-1 (29F.1A12), TIM3
681 (RMT3-23), CD4 (RM4-5), NK1.1 (PK136), CD19 (6D5), GZMB (GB12). Viability was
682 accessed by staining with LIVE/DEAD Fixable Dye (Thermo).

683

684 *Urinary detection of therapeutic response and resistance to ICB therapy*

685 At 3 hours after administration of ICB antibody-sensor conjugates, urine was collected
686 and analyzed for noninvasive detection of therapeutic response and resistance. FITC
687 reporters were isolated from urine samples using Dynabeads (Thermo) decorated with
688 αFITC antibody (Genetex). Sample fluorescence was measured by Cytation 5 plate
689 reader (Biotek), and reporter concentrations were determined by using a known FITC
690 ladder. Concentrations of isobaric mass reporters were quantified by Syneous Health
691 (Morrisville, NC) using LC-MS/MS.

692

693 *Cas9 knockout of B2m and Jak1.*

694 CRISPR guide RNA's were designed to target two exons in either B2m or Jak1 in the Mus
695 musculus GRCm38 genome. Top and bottom guide oligonucleotides were annealed
696 using T4 PNK (NEB) and ligated into the backbone of eSpCas9_PuroR_GFP plasmid
697 (Sigma) using BbsI cut sites and T7 ligase (NEB). $1x10^5$ MC38 cells were transfected
698 with gRNA-ligated eSpCas9 plasmids for 48 hours using TransIT-LT1 transfection
699 reagent (Mirus Bio) in Opti-MEM (Thermo Fisher) and cultured for 3 passages in DMEM
700 supplemented with 10% FBS and 1% penicillin-streptomycin (D10). Selection of
701 transfected cells were done by supplementing culture media with 2 ug/mL puromycin
702 (Thermo Fisher). Cells incubated with B2m-directed guides were stained with anti-mouse
703 H-2Kb (clone AF6-88.5). H-2Kb-negative GFP-positive cells were sorted into single cells
704 on a 96-well plate using FACSAria Fusion (BD Biosciences) and cultured for 2-3 weeks

in D10. For cells incubated with Jak1-directed guides, GFP-positive cells were sorted into single cells and cultured for 2-3 weeks in D10. Clones that passed the functional assays for successful deletion of B2m or Jak1 are selected for tumor studies.

In vitro validation.

DNA was isolated from single-cell WT and knockout clones, and a PCR reaction was done to amplify the edited regions within B2m and Jak1 exons. The PCR products were sequenced by Sanger sequencing, and sequencing results were analyzed with TIDE (Tracking of Indels by Decomposition) analysis (ref) to confirm knockout efficiency. WT and knockout tumor cells were stained for H2-Kb (clone AF6-88.5) to confirm the functional loss of B2m. WT and $B2m^{-/-}$ were pulsed with SIINFEKL (30 uM peptide concentration), washed, and coincubated with plate-activated OT1 T cells at 5:1 ratio of effector:target cell. After overnight incubation, cells were washed and stained for CD8 (53-6.7), IFNγ (XMG1.2), and GzmB (GB12). For IFNγ stimulation assay, WT and knockout tumor cells were incubated with recombinant murine IFNγ (Peprotech; 500 EU/mL) for 2 days and stained for surface expression of H2-Kb (AF6-88.5) and PD-L1 (10F.9G2).

Tumor RNA isolation and sequencing.

Mice bearing WT, $B2m^{-/-}$, $Jak1^{-/-}$ MC38 tumors were treated with either αPD1 or IgG1 (100 ug) every 3 or 4 days. After the third administration, approximately 50 mg of tumors were dissected and rapidly frozen with dry ice and IPA. Frozen tumor samples were homogenized in MACS M Tubes (Miltenyi) using the MACS Dissociator (Miltenyi). Total RNA was isolated from the homogenate using the RNeasy Plus Mini Kit (Qiagen). Library preparation with TruSeq RNA Library Prep Kit (Illumina) and mRNA NSG sequencing ($40x10^6$ paired end read) were performed by Admera Health (South Plainfield, NJ).

RNA-seq data mapping and visualization.

Raw FASTQ reads passing quality control (FastQC v0.11.2) were aligned on the mm10 reference genome using STAR aligner (v2.5.2a) with default parameters. Aligned fragments were then counted and annotated using Rsamtools (v3.2) and Cufflinks (v.2.2.1) after a 'dedup' step using BamUtils (v1.0.11). t-SNE embedding results were performed in sklearn (v0.23.1) using all murine genes. Heat maps were plotted with seaborn's (v.0.9.0) clustermap function. Rows were gaussian normalized, and the dendrograms shown for clustering come from hierarchical clustering using Euclidean distance as a metric.

Differential expression and gene set enrichment analysis.

Differential expression was performed using the edgeR package (v3.24.3) in R using the exactTest method with tagwise dispersion. For mouse data, TMM normalization considering mice in all treatment groups was performed to remove library size effect

through the calcNormFactors function. For human data[24], TMM normalization was performed using the two groups being compared. For both datasets, differential expression was performed on Ensembl IDs before mapping to gene names. Then the identified differentially expressed genes were filtered by a list of extracellular and transmembrane endopeptidases queried from UniProt. Gene set enrichment analysis (GSEA) was performed using the fgsea package (v1.8.0) in R. To rank genes, differential expression analysis was first performed on the entire gene set. Genes are then ranked by -sign(logFC)*log(pval). Hallmark gene sets (MSigDB) were used for all GSEA analyses.

Peptide substrate synthesis.

To optimize peptide substrates for target proteases, a library of potential substrates flanked by 5FAM fluorescent dye and DABCYL quencher (5FAM-substrate-Lys{DABCYL}-Amide) was synthesized by Genscript or manufactured in-house using Liberty Blue peptide synthesizer (CEM). The peptide synthesis scale used was 0.025 mM, and Low-loading rink amide resin (CEM) was used. Amino acids (Chem-Impex) were resuspended in DMF (0.08 M), as were all synthesis buffers. Activator buffer used was Diisopropylcarbodiimide (DIC; Sigma) (0.25 M) and the activator base buffer was Oxyma (0.25 M; CEM) while the deprotection buffer was Piperidine (20%; Sigma) supplemented with Oxyma (0.1 M). Crude peptides were purified on 1260 Infinity II HPLC system (Agilent) until a purity of 80% was achieved. Peptide mass and purity were validated by LC/MS (Agilent) and Autoflex TOF mass spectrometer (Bruker).

Protease substrate library optimization.

Fluorescently quenched peptide substrates (10 uM) were incubated in manufacturer-recommended buffers at 37°C with recombinant proteases (25 nM). Our set of human recombinant proteases included Granzyme A, Granzyme B, MMP1, MMP3, MMP7, MMP9, MMP13, Caspase 1, Caspase 3, Cathepsin G, Cathepsin S (Enzo), human thrombin, human Factor XIa (HaemTech), C1R, Fibroblast Activation Protein alpha/FAP, t-Plasminogen Activator/tPA Protein, and u-Plasminogen Activator/Urokinase (R&D systems). Sample fluorescence (Ex/Em = 488 nm/525 nm) were measured for 180 minutes using Cytation 5 plate reader (Biotek). Enzyme cleavage rates were quantified as relative fluorescence increase over time normalized to fluorescence before addition of protease. Hierarchical clustering was performed in python, using log2 fluorescence fold change at 60 minutes. A positive cleavage event was defined as having fluorescence signal more than 2-fold above background. Correlation analysis with Spearman coefficient was done on the cleavage patterns of all peptide substrates for selection of 14 substrates for library construction. These peptide substrates were paired with isobaric mass reporters based on the GluFib peptide (Table 1) and synthesized using Liberty Blue peptide synthesizer (CEM).

Urinary differentiation of ICB resistant mechanisms.

Random forest was used to train classifiers based on urinary reporter signals that differentiate therapeutic response and stratify resistant mechanisms. Response monitoring classifiers were trained on reporter concentration whereas resistance stratifying classifiers were trained on mean normalized reporter concentration. All urine signals were normalized on a per mouse basis by signals on the first dose to performed paired sample analyses. For each classification task, we used five-fold cross validation by randomly left out $1/5^{th}$ samples as the test set and used the remaining samples as training sets. This process was repeated 100 times, and the final performance was generated as the average area under the ROC curve (AUROC) for all train-test results.

Software and Statistical Analysis

Graphs were plotted and appropriate statistical analyses were conducted using GraphPad Prism (*P< 0.05, **P < 0.01, ***P < 0.001, ****P < 0.0001; central values depict the means, and error bars depict s.e.m.). Flow cytometry data were analyzed using FlowJo X (FlowJo, LLC). Power analyses were performed using G*Power 3.1 (HHUD).

Data availability

All data supporting the findings of this study are available in the manuscript and its Supplementary Information. Requests for raw data can be addressed to the corresponding authors.

References

1. Ribas, A. & Wolchok, J. D. Cancer immunotherapy using checkpoint blockade. *Science* **359**, 1350–1355 (2018).
2. Sharma, P. & Allison, J. P. The future of immune checkpoint therapy. *Science* **348**, 56–61 (2015).
3. Sharma, P., Hu-Lieskovan, S., Wargo, J. A. & Ribas, A. Primary, Adaptive, and Acquired Resistance to Cancer Immunotherapy. *Cell* **168**, 707–723 (2017).
4. Nishino, M., Ramaiya, N. H., Hatabu, H. & Hodi, F. S. Monitoring immune-checkpoint blockade: response evaluation and biomarker development. *Nat. Rev. Clin. Oncol.* **14**, 655–668 (2017).
5. Wolchok, J. D. *et al.* Guidelines for the Evaluation of Immune Therapy Activity in Solid Tumors: Immune-Related Response Criteria. *Clin. Cancer Res.* **15**, 7412–7420 (2009).
6. Bruni, D., Angell, H. K. & Galon, J. The immune contexture and Immunoscore in cancer prognosis and therapeutic efficacy. *Nat. Rev. Cancer* 1–19 (2020) doi:10.1038/s41568-020-0285-7.
7. Kalbasi, A. & Ribas, A. Tumour-intrinsic resistance to immune checkpoint blockade. *Nat. Rev. Immunol.* 1–15 (2019) doi:10.1038/s41577-019-0218-4.
8. Kessenbrock, K., Plaks, V. & Werb, Z. Matrix Metalloproteinases: Regulators of the Tumor Microenvironment. *Cell* **141**, 52–67 (2010).
9. Martínez-Lostao, L., Anel, A. & Pardo, J. How Do Cytotoxic Lymphocytes Kill Cancer Cells? *Clin. Cancer Res.* **21**, 5047–5056 (2015).

10. Kwong, G. A. *et al.* Mass-encoded synthetic biomarkers for multiplexed urinary monitoring of disease. *Nat. Biotechnol.* **31**, 63–70 (2013).
11. Dudani, J. S., Ibrahim, M., Kirkpatrick, J., Warren, A. D. & Bhatia, S. N. Classification of prostate cancer using a protease activity nanosensor library. *Proc. Natl. Acad. Sci. U. S. A.* **115**, 8954–8959 (2018).
12. Whitley, M. J. *et al.* A mouse-human phase 1 co-clinical trial of a protease-activated fluorescent probe for imaging cancer. *Sci. Transl. Med.* **8**, 320ra4-320ra4 (2016).
13. Rooney, M. S., Shukla, S. A., Wu, C. J., Getz, G. & Hacohen, N. Molecular and genetic properties of tumors associated with local immune cytolytic activity. *Cell* **160**, 48–61 (2015).
14. Larimer, B. M. *et al.* Granzyme B PET Imaging as a Predictive Biomarker of Immunotherapy Response. *Cancer Res.* **77**, 2318–2327 (2017).
15. LaSalle, T. *et al.* Granzyme B PET imaging of immune-mediated tumor killing as a tool for understanding immunotherapy response. *J. Immunother. Cancer* **8**, e000291 (2020).
16. Allen, E. M. V. *et al.* Genomic correlates of response to CTLA-4 blockade in metastatic melanoma. *Science* **350**, 207–211 (2015).
17. Desnoyers, L. R. *et al.* Tumor-Specific Activation of an EGFR-Targeting Probody Enhances Therapeutic Index. *Sci. Transl. Med.* **5**, 207ra144-207ra144 (2013).
18. Mac, Q. D. *et al.* Non-invasive early detection of acute transplant rejection via nanosensors of granzyme B activity. *Nat. Biomed. Eng.* **3**, 281–291 (2019).
19. Efremova, M. *et al.* Targeting immune checkpoints potentiates immunoediting and changes the dynamics of tumor evolution. *Nat. Commun.* **9**, 32 (2018).

20. Strohl, W. R. Fusion Proteins for Half-Life Extension of Biologics as a Strategy to Make Biobetters. *BioDrugs* **29**, 215–239 (2015).
21. Hu, Q. *et al.* Conjugation of haematopoietic stem cells and platelets decorated with anti-PD-1 antibodies augments anti-leukaemia efficacy. *Nat. Biomed. Eng.* **2**, 831–840 (2018).
22. Boland, G. M. & Flaherty, K. T. Tracking early response to immunotherapy. *Nat. Cancer* **1**, 160–162 (2020).
23. Sabio, E. & Chan, T. A. The good, the bad, and the ugly: hyperprogression in cancer patients following immune checkpoint therapy. *Genome Med.* **11**, (2019).
24. Riaz, N. *et al.* Tumor and Microenvironment Evolution during Immunotherapy with Nivolumab. *Cell* **171**, 934-949.e16 (2017).
25. Duraiswamy, J., Kaluza, K. M., Freeman, G. J. & Coukos, G. Dual Blockade of PD-1 and CTLA-4 Combined with Tumor Vaccine Effectively Restores T-Cell Rejection Function in Tumors. *Cancer Res.* **73**, 3591–3603 (2013).
26. Selby, M. J. *et al.* Preclinical Development of Ipilimumab and Nivolumab Combination Immunotherapy: Mouse Tumor Models, In Vitro Functional Studies, and Cynomolgus Macaque Toxicology. *PLOS ONE* **11**, e0161779 (2016).
27. Brinkman, E. K., Chen, T., Amendola, M. & van Steensel, B. Easy quantitative assessment of genome editing by sequence trace decomposition. *Nucleic Acids Res.* **42**, e168–e168 (2014).
28. Zaidi, M. R. The Interferon-Gamma Paradox in Cancer. *J. Interferon Cytokine Res.* **39**, 30–38 (2018).

29. Liberzon, A. *et al.* The Molecular Signatures Database Hallmark Gene Set Collection. *Cell Syst.* **1**, 417–425 (2015).
30. Dudani, J. S., Warren, A. D. & Bhatia, S. N. Harnessing Protease Activity to Improve Cancer Care. *Annu. Rev. Cancer Biol.* **2**, 353–376 (2018).
31. Buss, C. G., Dudani, J. S., Akana, R. T. K., Fleming, H. E. & Bhatia, S. N. Protease activity sensors noninvasively classify bacterial infections and antibiotic responses. *EBioMedicine* **38**, 248–256 (2018).
32. Lin, K. Y., Kwong, G. A., Warren, A. D., Wood, D. K. & Bhatia, S. N. Nanoparticles That Sense Thrombin Activity As Synthetic Urinary Biomarkers of Thrombosis. *ACS Nano* **7**, 9001–9009 (2013).
33. Kirkpatrick, J. D. *et al.* Urinary detection of lung cancer in mice via noninvasive pulmonary protease profiling. *Sci. Transl. Med.* **12**, (2020).
34. Waldman, A. D., Fritz, J. M. & Lenardo, M. J. A guide to cancer immunotherapy: from T cell basic science to clinical practice. *Nat. Rev. Immunol.* 1–18 (2020) doi:10.1038/s41577-020-0306-5.
35. Stephanopoulos, N. & Francis, M. B. Choosing an effective protein bioconjugation strategy. *Nat. Chem. Biol.* **7**, 876–884 (2011).
36. Khongorzul, P., Ling, C. J., Khan, F. U., Ihsan, A. U. & Zhang, J. Antibody–Drug Conjugates: A Comprehensive Review. *Mol. Cancer Res.* **18**, 3–19 (2020).
37. Galvani, E. *et al.* Stroma remodeling and reduced cell division define durable response to PD-1 blockade in melanoma. *Nat. Commun.* **11**, 853 (2020).
38. Havel, J. J., Chowell, D. & Chan, T. A. The evolving landscape of biomarkers for checkpoint inhibitor immunotherapy. *Nat. Rev. Cancer* **19**, 133–150 (2019).

39. Robert, C. *et al.* Pembrolizumab versus Ipilimumab in Advanced Melanoma. *N. Engl. J. Med.* **372**, 2521–2532 (2015).

40. Khoja, L., Butler, M. O., Kang, S. P., Ebbinghaus, S. & Joshua, A. M. Pembrolizumab. *J. Immunother. Cancer* **3**, 36 (2015).

41. Hayes, D. F. Biomarker validation and testing. *Mol. Oncol.* **9**, 960–966 (2015).

42. Riethdorf, S., O'Flaherty, L., Hille, C. & Pantel, K. Clinical applications of the CellSearch platform in cancer patients. *Adv. Drug Deliv. Rev.* **125**, 102–121 (2018).

Figures

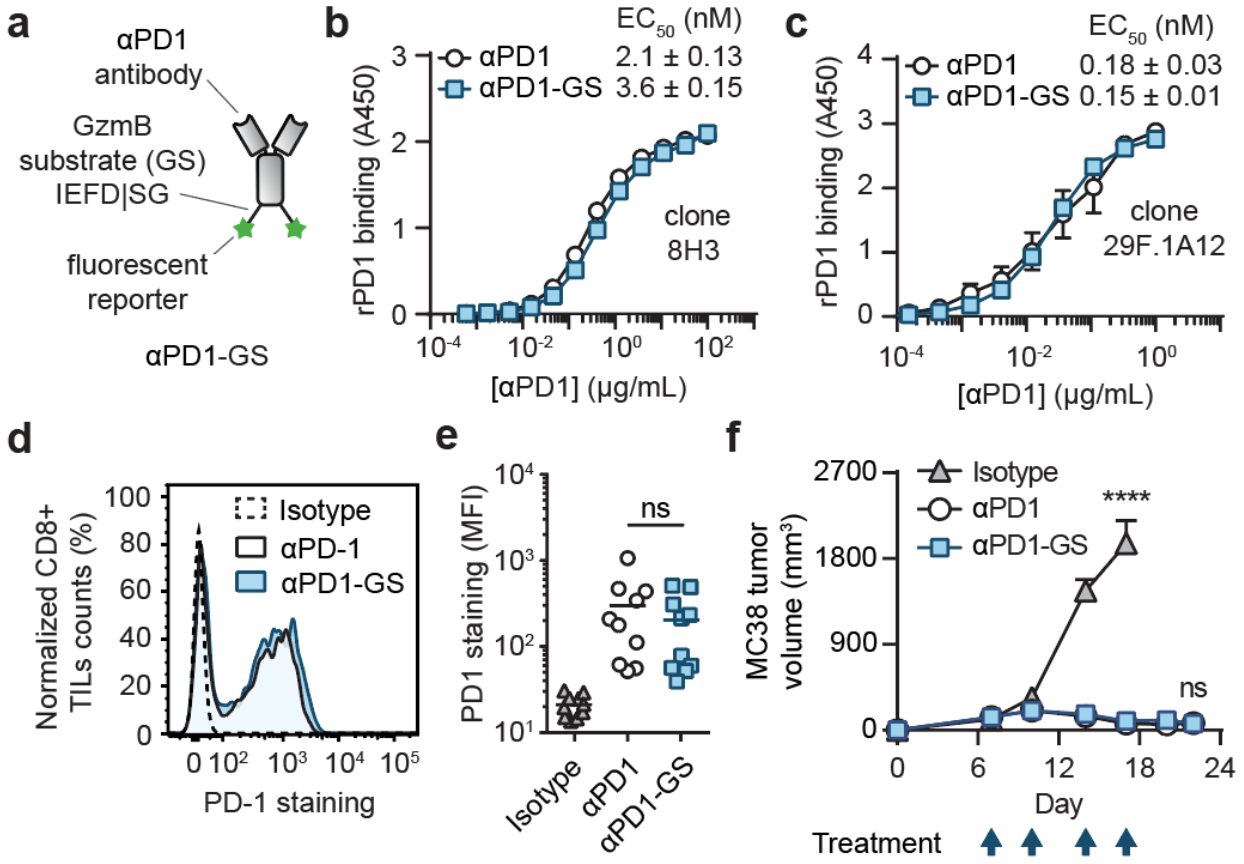

Figure 1 | Antibody binding and therapeutic efficacy are unaffected by peptide conjugation. **a**, αPD1-GzmB sensor conjugates (αPD1-GS) consists of αPD1 therapeutic antibody decorated with reporter-labeled GzmB peptide substrates (GS; AA sequence: IEFDSG). **b**, ELISA assays comparing binding affinity of αPD1-GS with unconjugated αPD1 using the mouse αPD1 clone 8H3 (log(agonist) vs. normalized response fitting function, n = 3). **c**, ELISA assays comparing binding affinity of αPD1-GS with unconjugated αPD1 using the rat αPD1 clone 29F.1A12 (log(agonist) vs. normalized response fitting function, n = 3). **d**, Flow cytometry histogram showing PD-1 expression of CD8+ TILs isolated from MC38 tumors. The same sample was divided and stained with either αPD1-GS, αPD1, or IgG1 isotype control. **e**, Quantified plot of PD-1 expression

showing the median fluorescence intensity (MFI) of samples stained with either αPD1-GS, αPD1, or IgG1 isotype control (one-way ANOVA with Turkey's post-test and correction for multiple comparisons, ns = not significant, n = 10). **f**, Tumor growth curves of MC38 tumors treated with αPD1-GS, αPD1, or IgG1 isotype control (two-way ANOVA with Turkey's post-test and correction for multiple comparison, ****P < 0.0001, n = 6).

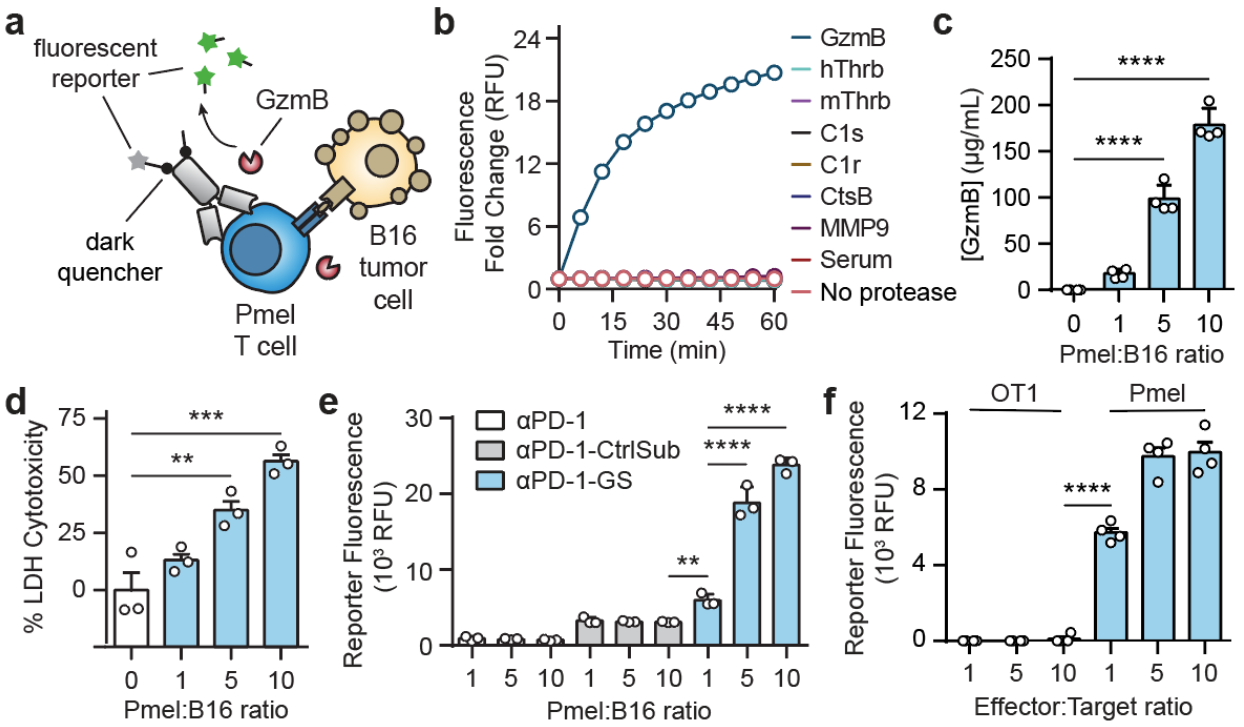

Figure 2 | Sensing T cell killing of tumor cells by antibody-GzmB sensor conjugates. **a**, αPD1 antibody was conjugated with fluorescently-quenched peptide substrates for GzmB. Upon incubating these conjugates with transgenic Pmel T cells and B16 tumor cells, secreted GzmB cleaved peptide substrates, separating the fluorescent reporter from the internal quencher, resulting in an increase in sample fluorescence. **b**, *In vitro* protease cleavage assays showing normalized fluorescence of αPD1-GS after incubation with recombinant GzmB (blue), mouse serum (red), and other bystander proteases (n = 3). **c**, ELISA quantification of GzmB from T cell killing assays in which Pmel T cells were incubated with B16 target cells at different T cell to target cell ratios (one-way ANOVA with Dunnett's post-test and correction for multiple comparisons, ****P < 0.0001, n = 4). **d**, Bar plot quantifying percent of cell cytotoxicity as measured by LDH assay from cocultures of Pmel T cells with B16 target cells (one-way ANOVA with Dunnett's post-test and correction for multiple comparisons, ***P < 0.001, n = 3). **e**,

Activity assays showing sample fluorescence after incubating αPD1-GS, αPD1, and an αPD1 conjugate with control substrates (αPD1-CtrlSub) with cocultures of Pmel T cells with B16 target cells (two-way ANOVA with Turkey's post test and correction for multiple comparisons, ****P < 0.0001, n = 3). **f**, Activity assays showing sample fluorescence after incubating αPD1-GS with cocultures of Pmel or OT1 transgenic T cells with B16 target cells (two-way ANOVA with Turkey's post test and correction for multiple comparisons, ****P < 0.0001, n = 3).

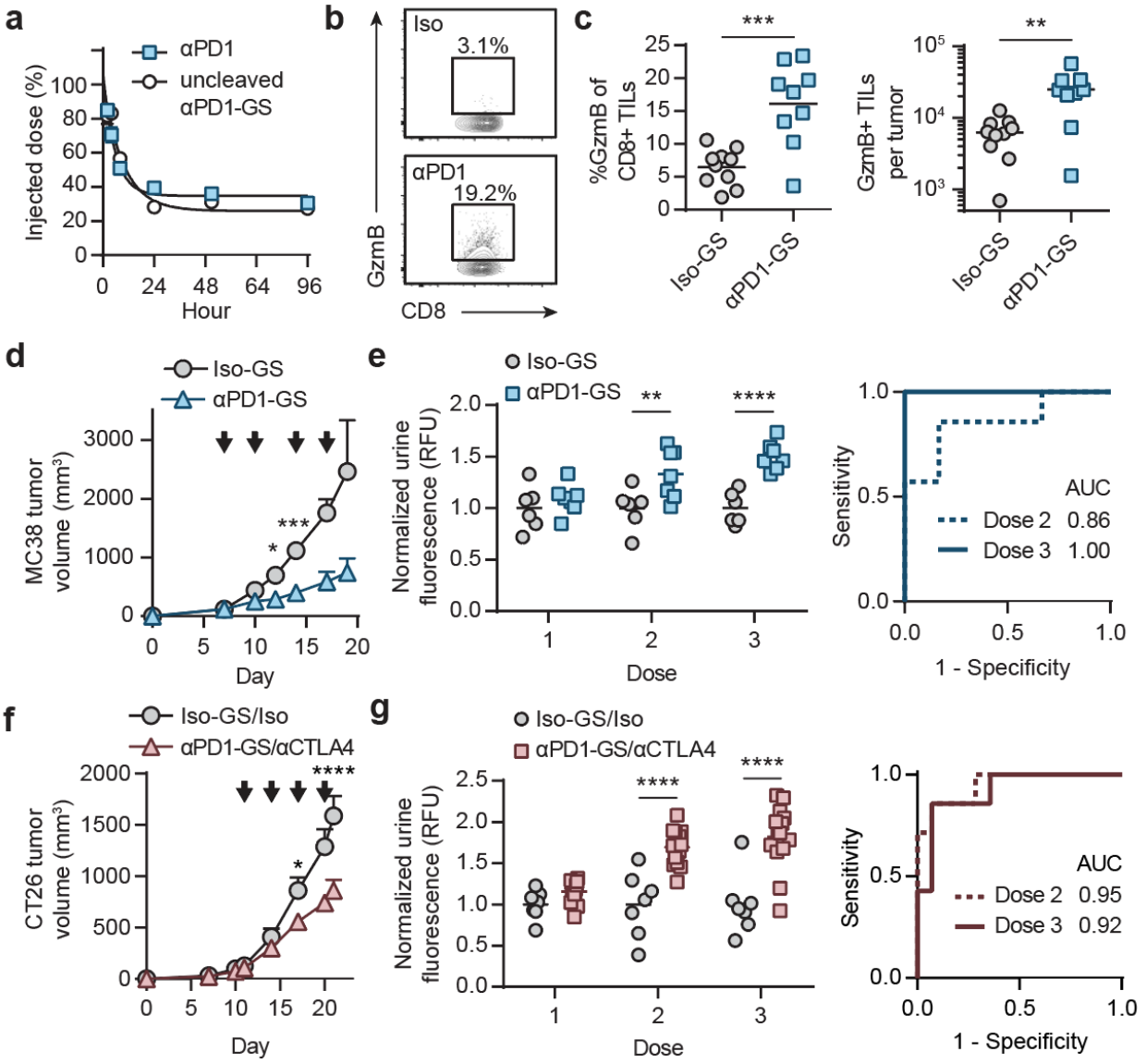

Fig 3 | Urinary detection of ICB therapeutic response by administration of antibody-GzmB sensor conjugates. **a**, Half-life measurements of intact αPD1-GS and unconjugated αPD1 antibody (one phase decay fitting function, n = 3). **b**, Flow cytometry plots showing intracellular GzmB expression of CD8+ TILs from MC38 tumors treated with either αPD1-GS or IgG1 isotype antibody conjugated with the GzmB peptide substrates (Iso-GS). **c**, Quantified plots showing percentages of GzmB+ cells within the CD8+ TILs or the numbers of GzmB+CD8+ TILs that were isolated from MC38 tumors treated with either αPD1-GS or Iso-GS (two-sided Student's t-test, n = 9-10). **d**, Tumor

growth curves of MC38 tumor bearing mice treated with either αPD1-GS or Iso-GS (two-way ANOVA with Sidak's post test and correction for multiple comparisons, ***P < 0.001, n = 6-7). Black arrows denote the treatment time points. **e**, Left: normalized urine fluorescence of mice with MC38 tumors after each administration of αPD1-GS or Iso-GS (two-way ANOVA with Sidak's post test and correction for multiple comparisons, ****P < 0.0001, n = 6-7). Right: receiver-operating-characteristic (ROC) analysis showing the diagnostic specificity and sensitivity of αPD1-GS in differentiating between responders to αPD1 monotherapy from off-treatment controls using urine signals on the second (AUC = 0.857, 95% CI = 0.643-1.071) or the third dose (AUC = 1.00, 95% CI = 1.00-1.00). **f**, Tumor growth curves of CT26 tumor bearing mice treated with combination therapy of αPD1-GS and αCTLA4 or combination of matched isotype controls (two-way ANOVA with Sidak's post test and correction for multiple comparisons, ****P < 0.0001, n = 7-14). Black arrows denote the treatment time points. **g**, Left: normalized urine fluorescence of mice with CT26 tumors after each administration of αPD1-GS and αCTLA4 or matched isotype controls (two-way ANOVA with Sidak's post test and correction for multiple comparisons, ****P < 0.0001, n = 7-14). Right: receiver-operating-characteristic (ROC) analysis showing the diagnostic specificity and sensitivity of αPD1-GS in differentiating between responders to ICB combination therapy from off-treatment controls using urine signals on the second (AUC = 0.949, 95% CI = 0.856-1.042) or the third dose (AUC = 0.92, 95% CI = 0.795-1.042)

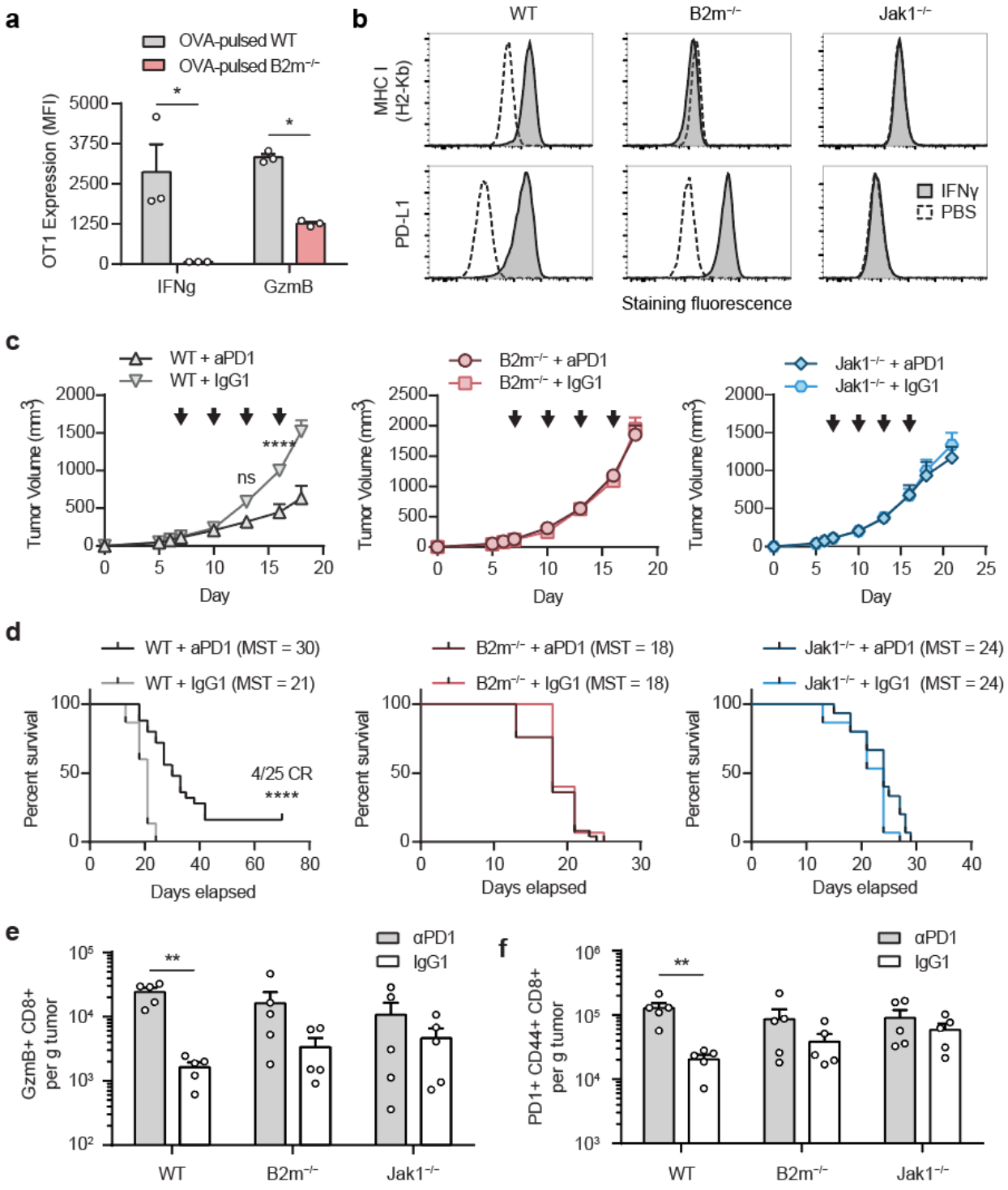

Figure 4 | Loss of function mutations in B2m and Jak1 rendered MC38 tumors resistant to αPD1 monotherapy. **a**, Bar plots showing median fluorescence intensity (MFI) of T cell effector molecules IFNγ and GzmB expressed by OT1 transgenic T cells

in cocultures with wildtype (WT) or B2m$^{-/-}$ MC38 tumor cells pulsed with the cognate antigen ovalbumin (OVA) (two-tailed Student's t-test, n = 3). **b**, Flow cytometry histograms showing expression of MHC-I (H2-Kb) and PD-L1 on the surface of WT, B2m$^{-/-}$, and Jak1$^{-/-}$ MC38 tumor cells upon stimulation with either IFNγ or PBS. **c**, Tumor growth curves of mice bearing WT (left), B2m$^{-/-}$ (middle), or Jak1$^{-/-}$(right) MC38 tumor treated with αPD1 or matched IgG1 control (two-way ANOVA with Sidak's post test and correction for multiple comparisons, ****P < 0.0001, n = 15-25). Black arrows denote the treatment time points. **d**, Survival curves of mice bearing WT (left), B2m$^{-/-}$ (middle), or Jak1$^{-/-}$(right) MC38 tumor treated with αPD1 or matched isotype control (Log-rank (Mantel-Cox) test, n = 15-25). **e**, **f**, Quantified plots of flow cytometry data showing the number of GzmB+ CD8+ TILs or PD1+ CD44+ CD8+ TILs per 1 gram of tumors from mice bearing WT, B2m$^{-/-}$, or Jak1$^{-/-}$ MC38 tumor treated with αPD1 or matched isotype control (two-way ANOVA with Sidak's post test and correction for multiple comparison, **P < 0.01, n = 5).

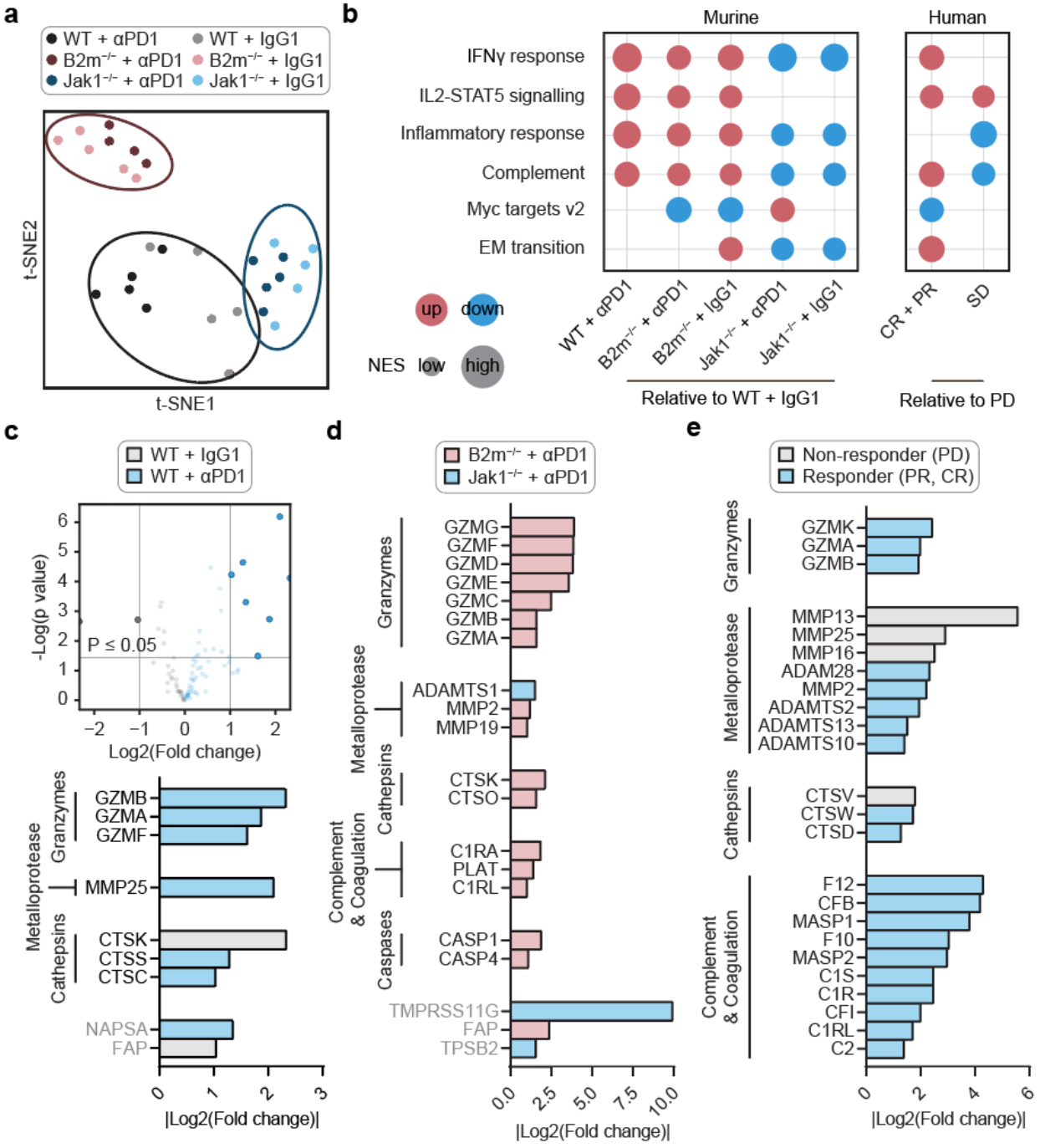

Figure 5 | Proteases are differentially regulated in ICB response and resistance. a, t-SNE plot showing global transcriptional profiles of WT, B2m$^{-/-}$, and Jak1$^{-/-}$ MC38 tumors treated with αPD1 or IgG1 isotype control (n = 5). **b**, Left: GSEA comparing gene set signatures of all mouse tumors and treatment groups relative to WT tumors receiving

isotype control treatment (n = 5). 6 gene sets were shown from the canonical Hallmark gene sets[29], with 4 immune- and 2 tumor-associated gene sets. Only the gene sets that are significantly different (FDR < 0.05) between the two groups being compared were shown. Red color indicates upregulation in the first group, and blue indicates downregulation. The size of the circle represents the nominal enrichment score (NES). Right: similar GSEA analyses using human data from melanoma patients treated with αPD1 monotherapy[24]. Gene set signatures of the two patient groups (Complete Response (CR) + Partial Response (PR), and Stable Disease (SD) were compared to patients with Progressive Disease (PD). **c**, Top: Volcano plots summarizing the extracellular and transmembrane proteases differentially expressed between WT MC38 tumors treated with αPD1 or IgG1 (n = 5). The threshold for differentially expressed genes (opaque dots) was defined as P value ≤ 0.05 and |log2(fold change)| ≥ 1. Bottom: waterfall plot showing the fold changes in transcript levels of proteases that are differentially expressed between these two groups. The proteases are grouped into the families of interest while the remaining are greyed out. **d**, Waterfall plot showing the fold changes in transcript levels of proteases that are differentially expressed between αPD1 treated $B2m^{-/-}$ and $Jak1^{-/-}$ tumors (n = 5). **e**, Waterfall plot showing the fold changes in transcript levels of proteases that are differentially expressed between human tumors from responders (CR + PR) and non-responders (PD).

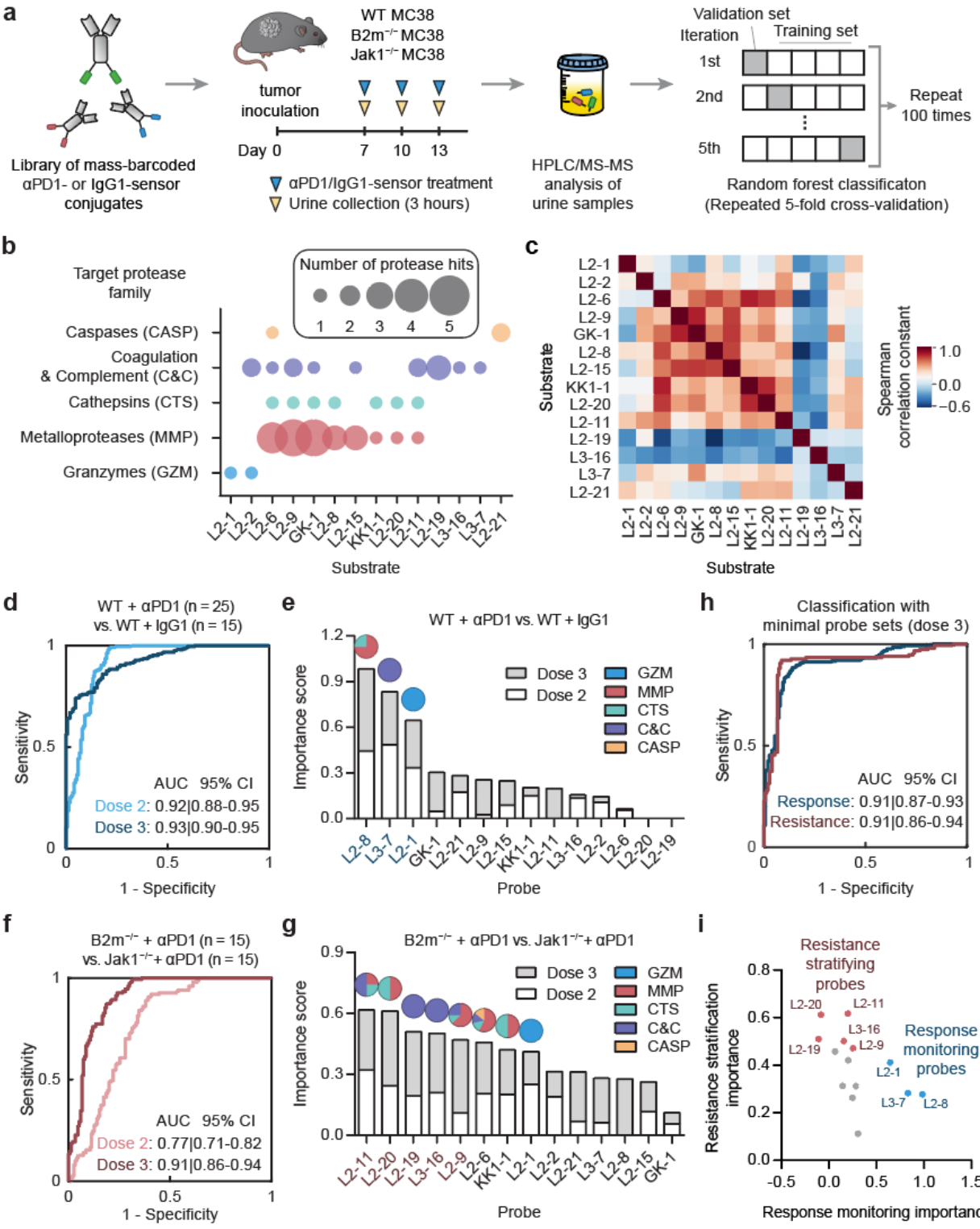

Figure 6 | Urinary classification of ICB response and resistance. a, Schematics of our pipeline to develop urinary classifiers of ICB response and resistance. **b**, Bubble plot

showing the numbers of protease hits per target protease family for each substrate in the INSIGHT multiplexed panel. A positive protease hit was defined as having average probe fluorescence at 60 min post protease addition at least 2-fold above background signals. **c**, Correlation matrix showing the Spearman correlation between the protease cleavage patterns of 14 peptide substrates in the INSIGHT panel. **d**, Area under the ROC curve analysis showing the diagnostic specificity and sensitivity of random forest classifiers based on INSIGHT library in differentiating between αPD1-treated WT tumors (n = 25) from IgG1-treated controls (n = 15) using urine signals on the second (AUC = 0.92, 95% CI = 0.88-0.95) or the third dose (AUC = 0.93, 95% CI = 0.90-0.95). **e**, Feature importance analysis revealing the probes that are important for the response monitoring. Probes with higher important scores, produced by random forest, have more important contribution to the diagnostic performance. The pie charts above individual probes showing the protease families that could be monitored by each probe. **f**, Area under the ROC curve analysis showing the diagnostic specificity and sensitivity of random forest classifiers based on INSIGHT library in differentiating between αPD1-treated $B2m^{-/-}$ (n = 15) from $Jak1^{-/-}$ MC38 (n = 15) tumors using urine signals on the second (AUC = 0.77, 95% CI = 0.71-0.82) or the third dose (AUC = 0.91, 95% CI = 0.86-0.94). **g**, Feature importance analysis revealing the probes that are important for resistance stratification. **h**, Area under the ROC curve analysis showing the diagnostic specificity and sensitivity of random forest classifiers based on the minimal set of 3 probes (L2-8, L3-7, L2-1) for response monitoring (AUC = 0.91, 95% CI = 0.87-0.93) and on the set of 5 probes (L2-11, L2-20, L2-19, L3-16, and L2-9) for resistance stratification (AUC = 0.91, 95% CI = 0.86-0.94). i, Scatter plot showing feature important scores of all 14 probes in the INSIGHT panel for response

monitoring and resistance stratification. The highlighted probes belong to the minimal probe sets that achieve comparable diagnostic performance in these classification tasks as compared to when using the entire panel.